

Research article

Jeffrey J. Schwartz, Son T. Le, Sergiy Krylyuk, Curt A. Richter, Albert V. Davydov and Andrea Centrone*

Substrate-mediated hyperbolic phonon polaritons in MoO₃

<https://doi.org/10.1515/nanoph-2020-0640>

Received December 4, 2020; accepted January 27, 2021;
published online February 15, 2021

Abstract: Hyperbolic phonon polaritons (HPhPs) are hybrid excitations of light and coherent lattice vibrations that exist in strongly optically anisotropic media, including two-dimensional materials (e.g., MoO₃). These polaritons propagate through the material's volume with long lifetimes, enabling novel mid-infrared nanophotonic applications by compressing light to sub-diffractive dimensions. Here, the dispersion relations and HPhP lifetimes (up to ≈ 12 ps) in single-crystalline α -MoO₃ are determined by Fourier analysis of real-space, nanoscale-resolution polariton images obtained with the photo-thermal induced resonance (PTIR) technique. Measurements of MoO₃ crystals deposited on periodic gratings show longer HPhPs propagation lengths and lifetimes ($\approx 2\times$), and lower optical compressions, in suspended regions compared with regions in direct contact with the substrate. Additionally, PTIR data reveal MoO₃ subsurface defects, which have a negligible effect on HPhP

propagation, as well as polymeric contaminants localized under parts of the MoO₃ crystals, which are derived from sample preparation. This work highlights the ability to engineer substrate-defined nanophotonic structures from layered anisotropic materials.

Keywords: 2D materials; hyperbolic materials; phonon polaritons; photothermal induced resonance; sub-wavelength optical confinement.

1 Introduction

The ability to confine and to guide light at length scales smaller than its free-space wavelength (λ_0) enables numerous nanophotonic applications, including surface-enhanced absorption and scattering [1–5], nanoscale waveguides [6–8], and non-linear optics [9, 10]. Polaritons, hybrid excitations of light and coherent charge oscillations in materials, offer a means to achieve such optical control at the nanoscale. For example, several spectroscopic techniques utilize surface plasmon polaritons (SPPs) in metals to boost their sensitivities [2, 11, 12]. However, the fast carrier scattering times in metals (\approx fs) results in high losses that generally hinder many nanophotonic applications, especially in the mid-infrared (mid-IR) [13, 14].

Phonon polaritons (PhPs), by contrast, couple light with optical phonons in a polar crystal. These excitations can exist only within spectral ranges, known as reststrahlen bands, delimited by transverse optical (TO) and longitudinal optical (LO) phonon pairs [14, 15]. Within these bands, at least one component of the material's electric permittivity tensor is negative, resulting in high optical reflectivity while supporting surface-bound PhP modes. Strongly anisotropic materials, in which the real permittivity differs in sign along orthogonal principal axes, support hyperbolic PhPs (HPhPs) within the material's volume, propagating at angles determined by the wavelength-dependent permittivity [14, 16, 17]. Such hyperbolic materials, therefore, enable high optical

*Corresponding author: **Andrea Centrone**, Physical Measurement Laboratory, National Institute of Standards and Technology, Gaithersburg, MD 20899, USA, E-mail: andrea.centrone@nist.gov. <https://orcid.org/0000-0002-2919-3366>

Jeffrey J. Schwartz, Physical Measurement Laboratory, National Institute of Standards and Technology, Gaithersburg, MD 20899, USA; and Institute for Research in Electronics and Applied Physics, University of Maryland, College Park, MD 20742, USA. <https://orcid.org/0000-0003-1544-1901>

Son T. Le, Physical Measurement Laboratory, National Institute of Standards and Technology, Gaithersburg, MD 20899, USA; and Theiss Research, La Jolla, CA 92037, USA

Sergiy Krylyuk and Albert V. Davydov, Material Measurement Laboratory, National Institute of Standards and Technology, Gaithersburg, MD 20899, USA. <https://orcid.org/0000-0003-4573-9151> (S. Krylyuk). <https://orcid.org/0000-0003-4512-2311> (A.V. Davydov)

Curt A. Richter, Physical Measurement Laboratory, National Institute of Standards and Technology, Gaithersburg, MD 20899, USA. <https://orcid.org/0000-0003-4510-1465>

confinements ($\approx 1\% \lambda_0$) in the mid-IR, with longer lifetimes (\approx ps) and lower losses compared with SPPs [14, 17–19]. Additionally, HPhPs provide the potential for negative refraction, superlensing, and other effects [16, 20, 21].

A number of natural hyperbolic materials supporting HPhPs have been discovered, including h-BN [22, 23] and MoO₃ [24–26], which have been the subject of recent reviews [27, 28]. Among these materials, MoO₃ is of particular interest due to its natural in-plane anisotropic dispersion [25]. To date, the optical dispersion relations in these materials have been predominantly determined by using scattering-type scanning near-field optical microscopy (s-SNOM) thanks to its ability to image HPhP propagation in real space with nanoscale resolution [20, 24, 29, 30]. Recently, similar investigations were accomplished with photoinduced force microscopy (PiFM) [26, 31, 32] and photothermal induced resonance (PTIR) [32–34], two nanoscale-capable IR techniques that do not require a spectrally sensitive detector in the far-field. In particular, PTIR was shown to detect a more complete set of theory-predicted HPhP modes in h-BN frustum structures [35, 36], revealing excitations not observed by s-SNOM. With PTIR, light absorption in a sample is measured by transducing the photo-induced thermal expansion of the sample directly beneath the probe tip of an atomic force microscope [37]. Notably, PTIR can sense sample composition far below the exposed surface [38–40], at depths exceeding 1 μ m [33, 41], with its signal proportional to the local sample absorption coefficient [42], enabling easy comparison of PTIR spectra with far-field IR databases [40, 42, 43]. These characteristics enable broad applications in materials science [44–46] and biology [47–51]. In nanophotonics, PTIR has been used to characterize integrated waveguides [52], plasmonic modes [53, 54], and near-field absorption enhancement of plasmonic nanostructures [55–57]. Here, we leverage PTIR to visualize HPhPs propagating in MoO₃ single-crystalline thin layers exfoliated on gold-coated glass or on SiO₂/Si substrates patterned into one-dimensional (1D) gratings. Fourier analyses of PTIR absorption maps and real-space parameterized models of HPhP propagation were used to determine the dispersion relations and to quantify lifetimes, propagation lengths, and optical compressions of HPhPs in MoO₃ single crystals. Increased HPhP propagation lengths and lifetimes of about 2 \times were observed in suspended regions of MoO₃ flakes compared with those in direct contact with SiO₂. In addition to demonstrating similar capabilities to s-SNOM, here we highlight the ability of PTIR to detect and to discern intrinsic (within MoO₃) and extrinsic (contaminants) subsurface defects.

Understanding and controlling the factors that influence HPhP propagation, as examined here, enhances the ability to engineer light–matter interactions at dimensions below the diffraction limit, which is critical for a variety of materials and nanophotonic applications.

2 Results and discussion

The structure of orthorhombic α -MoO₃ (Figure 1a) consists of stacked bilayers composed of distorted MoO₆ octahedra with three crystallographically inequivalent oxygen atoms [58]. Thanks to its layered, van der Waals type structure, single crystals of α -MoO₃ can be exfoliated into flakes of various thicknesses and sizes, with edges predominantly aligned with crystallographically defined [100] and [001] directions. Additionally, MoO₃ is characterized by numerous IR-active optical phonon modes, resulting in multiple reststrahlen bands that can support HPhP propagation [59]. Two of these bands, between about 820 and 972 cm^{-1} (“lower band”), and between about 958 and 1004 cm^{-1} (“upper band”) [24–26, 59], were probed in this work (for further reststrahlen band details see discussion S1 in Supplementary material).

The excitation of HPhPs typically requires the use of evanescent illumination geometries or light-scattering sites to bridge the momentum mismatch between incident photons in free space and polaritons within a material [14, 30]. Intrinsic features, such as crystal edges, or extrinsic ones, such as plasmonic nanostructures or the tip of a scanning probe microscope, commonly fulfill this role [30, 36]. For materials confined in at least one dimension, as in the case of the thin flakes studied here, HPhPs are permitted only with specific (quantized) momenta [35, 60], meaning that they propagate only at selected angles determined by the permittivity tensor of the material. Consequently, in s-SNOM and PTIR real-space maps, HPhPs appear as periodic fringes with spacing proportional to the flake thickness (Figure S1). The polariton fringes observed in PTIR measurements result from especially intense local heating and thermal expansion of the sample that occurs in regions where the strong tip-enhanced near-field overlaps with the polariton field [36]. Polaritons launched at crystal edges (“edge-launched”) propagate through the material with characteristic wavenumbers and are detected at the probe with corresponding spatial frequencies determined by the material dispersion. Similarly, light scattered by the probe tip generates “tip-launched” polaritons that emanate outward and are detected after reflecting back to the probe from another interface such as a flake edge. Both edge-launched and tip-

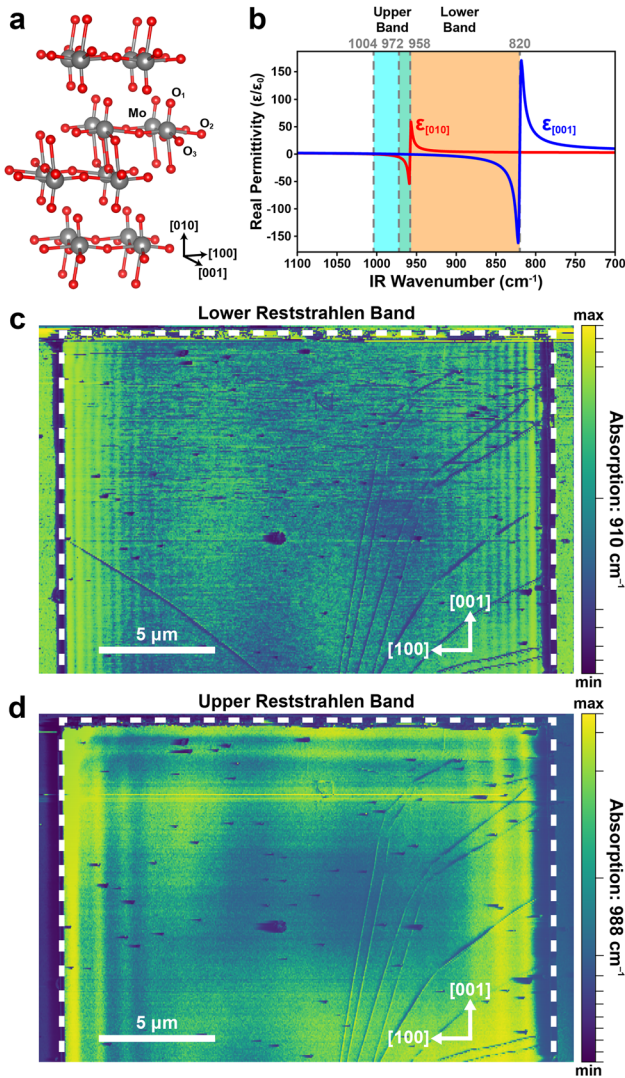


Figure 1: Photothermal induced resonance (PTIR) detects hyperbolic phonon polaritons (HPhPs) in a MoO₃ single crystal. (a) Crystal structure of orthorhombic α -MoO₃ (space group D_{2h}^{16} -Pbnm), depicting Mo (in gray) at the center of octahedra composed of three crystallographically inequivalent oxygen atoms (labeled “O₁,” “O₂,” and “O₃”) in red. (b) Real components of the complex electric permittivity tensor (ϵ), relative to that of free space (ϵ_0), along the [001] (blue line) and [010] (red line) crystallographic directions in MoO₃. The spectral regions highlighted with pale red and blue backgrounds represent the two, partially overlapping, reststrahlen bands probed in this work. Real-space PTIR absorption maps at (c) 910 cm⁻¹ and at (d) 988 cm⁻¹ of a MoO₃ flake (\approx 315 nm thick) deposited on a uniform, gold-coated glass substrate. Dashed lines depict the approximate locations of the flake edges. Polaritons in MoO₃ manifest as a superposition of periodic fringes of varying absorption intensity. The [100] and [001] crystallographic directions are inferred from the fringes observed in each reststrahlen band. Elliptic in-plane propagation (type I) is observed in the upper band, while hyperbolic in-plane propagation (type II) is observed in the lower band. Note that non-linear color scales are used, with bands of approximately equal change in absorption intensity indicated by tick marks along the right sides of the color bars. The topography map acquired simultaneously with (c) is available in the Supplementary material (Figure S2).

launched HPhPs can exist and be detected simultaneously in PTIR absorption maps, which capture a superposition of all excited modes. However, tip-launched polaritons are characterized by fringe periods that are approximately half that of edge-launched modes of the same order (see below) [61]. Depending on the relative excitation efficiencies of a particular sample, either tip- or edge-launched (or both) HPhPs may be prominently generated and observed. Nevertheless, tip- and edge-launched HPhPs are fundamentally the same phenomenon and their approximate 2:1 wavenumber ratio is just a consequence of the scanning probe measurement scheme (see below).

Representative PTIR absorption maps measured in two MoO₃ reststrahlen bands (Figure 1) reveal significant differences in HPhP propagation. In the lower band (Figure 1c), absorption fringes are aligned parallel to the left and right edges of the MoO₃ flake (nearly vertical) but no fringes are observed along the top (horizontal) edge of the flake. By contrast, in the upper reststrahlen band (Figure 1d), fringes parallel to all visible flake edges are observed, though with lower spatial frequencies than in the lower band. Additionally, in this case, interference between cross-propagating polaritons is evident, especially near the corners of the flake (e.g., Figure 1d, top-right). Such differences reflect the optical anisotropy of MoO₃ and the distinct hyperbolic characters of the two reststrahlen bands (upper band, type I; lower band type II), as observed previously in s-SNOM studies on SiO₂ substrates [24–26]. Therefore, PTIR images of HPhP propagation along flake edges can be used to identify the crystallographic orientation of the MoO₃ flake, which is indicated in Figure 1.

Real-space PTIR absorption maps encode information related to the superposition of all HPhP modes propagating in the hyperbolic material as variations (e.g., fringes) in the PTIR signal intensity. Discrete Fourier transforms (DFTs) of these real-space maps separate, in frequency space, the polaritons (peaks in the computed power spectra; see, e.g., Figure 2c) from the background absorption and other artifacts. Polaritons observed in this manner can be attributed either to edge- or tip-launched HPhPs propagating in the hyperbolic media, which we model here as damped harmonic oscillations.

For HPhPs propagating in one dimension along an x -coordinate axis, with angular wavenumber k and experiencing damping γ , we fit Equation (1) to the measured real-space absorption profiles.

$$\text{Absorption} \propto \sum_i A_i e^{-\gamma_i x} \cos(k_i x + \varphi_i) \quad (1)$$

In this model, a phase parameter (φ) accounts for offsets in the relative positions of the measurement origin (taken to

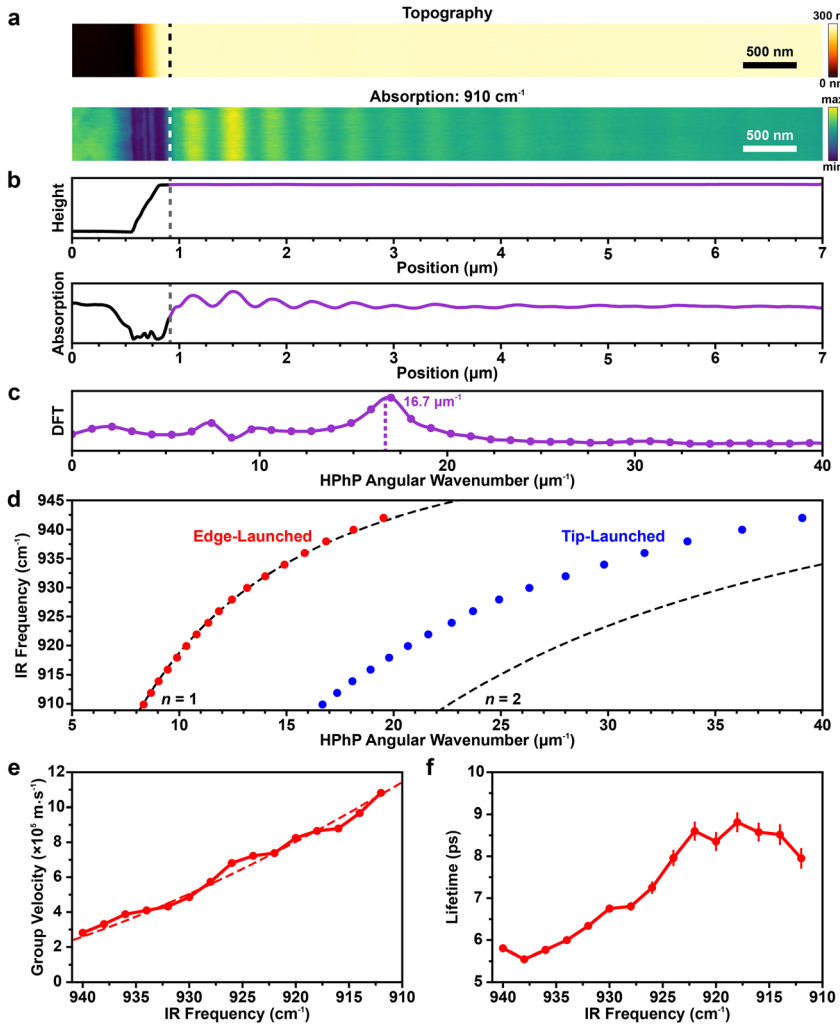


Figure 2: Real-space photothermal induced resonance (PTIR) imaging enables characterization of hyperbolic phonon polariton (HPhP) propagation.

(a) Topography (top) and PTIR absorption map (bottom) of a MoO₃ flake (approximately 279 nm thick) on a uniform, gold-coated glass substrate, illuminated at 910 cm⁻¹. (b) Average height (top) and absorption (bottom) line profiles from (a), scaled to arbitrary units. The dashed lines in (a) and (b) denote the position of the topographically identified flake edge; profile segments inside and outside the flake edge are shown in purple and in black, respectively. (c) Magnitude of the discrete Fourier transform (DFT) of the absorption line profile, within the interior of the flake only, showing a prominent peak representing a tip-launched HPhP mode. (d) Dispersion relation of HPhPs in the MoO₃ flake shown in (a). Dashed lines represent the theoretical HPhP dispersion (see Supplementary material S1.2) for edge-launched modes of order n . (e) Group velocities and the corresponding (f) lifetimes of the edge-launched HPhP modes from (d). Dashed line in (e) represents the derivative of the theoretical dispersion ($n = 1$) from (d). Error bars in (d–f) represent uncertainties in the mean values, propagated from least-squares fit covariance matrices.

be the topographically identified flake edge) and the fringe pattern, while A scales the model amplitude to match the measured intensities. Since, in general, PTIR absorption profiles represent superpositions of HPhPs, the model sums over i independent modes, which are identified by peaks (k) in their power spectra (see below and Figure 2c). By fitting this model to the PTIR absorption profiles we obtain estimates of the parameters (A_i , γ_i , k_i , φ_i) that characterize each mode. These parameters can be used to quantify the HPhP damping rates and lifetimes. This analysis is illustrated in Figure 2 for a MoO₃ flake with its edge aligned nearly perpendicular (vertical) to the fast-scan direction of the probe (horizontal). In this configuration, sequentially measured scan lines possess an approximate translational symmetry along the slow-scan direction of the probe (vertical). Consequently, column-wise (vertical) averaging of pixels in the resulting PTIR images enables 1D analyses with enhanced signal-to-noise ratios. The DFT power spectrum (Figure 2c) of the averaged, 1D absorption profile reveals a

prominent polariton peak ($\approx 16.7 \mu\text{m}^{-1}$). By plotting the angular wavenumbers of the detected DFT peaks (blue circles in Figure 2d) obtained from the Fourier analysis of a series of PTIR images, measured at different IR wavelengths, we constructed the HPhP dispersion curve of this MoO₃ crystal. Clearly, the measured polariton dispersion does not match the trend line predicted by theory for the first ($n = 1$) or second ($n = 2$) order edge-launched HPhP modes (dashed lines in Figure 2d); see theory details in Supplementary material S1.2. However, the measured angular wavenumbers are approximately double the values predicted for the first order edge-launched mode. Therefore, we attribute the prominent peaks in the DFT plots to HPhPs launched by the gold-coated probe tip [61]. For tip-launched HPhPs, movement of the probe toward or away from a flake edge changes the distance traversed by tip-launched HPhPs by twice that of the corresponding edge-launched HPhPs (see Equation (1)), leading to an apparent doubling of the spatial frequencies of HPhPs launched by the tip [61]. Scaling the

observed spatial frequencies by a factor of 1/2 enables reconstruction of the complementary edge-launched HPhP dispersion curve (red circles in Figure 2d), which coincides closely with theoretical predictions for edge-launched polaritons. The relative amplitudes of the tip- and edge-launched peaks in the DFT power spectra depend on the relative launching efficiencies and can vary between samples and scattering sites [30]. Typically, tip-launched HPhPs are assumed to originate from an azimuthally symmetric source (probe tip), and propagate outward with a circular wave front that decays in intensity proportional to an additional \sqrt{x} prefactor not shown in Equation (1) but accounted for in our fitting and subsequent analyses. For the remainder of this work, HPhP propagation characteristics are reported for the cases of edge-launched HPhPs, either observed directly or from scaled analyses of more prominently detected tip-launched HPhPs.

Additional HPhP characteristics can be derived from the model-fit parameters. Significantly, the damping factors describe the rates at which HPhPs decay in the material and can be related to their propagation lengths (L), as shown in Figure S3, using Equation (2).

$$L = \frac{1}{\gamma} \quad (2)$$

Additionally, the speed (group velocity, v_g) of HPhPs propagation through the material can be determined from the slope of the dispersion curve,

$$v_g = \frac{\partial \omega}{\partial k}, \quad (3)$$

which is shown in Figure 2e for HPhPs in the lower reststrahlen band. We note that HPhPs in MoO₃ [25], and other hyperbolic materials [14, 19], propagate with high optical compressions ($\approx 30\times$, $\lambda_{\text{HPhP}} \approx 3\% \lambda_0$) and at speeds much slower than the corresponding free-space photons; here, $v_g \approx 0.1\% c$, among the slowest reported values for such materials [25, 62]. Furthermore, HPhP lifetimes (τ) can be estimated from the approximate relationship between the propagation length and group velocity shown in Equation (4).

$$\tau \approx \frac{L}{v_g} \quad (4)$$

These characteristics enable quantitative comparisons of HPhP propagation in different materials and samples, thus permitting a comparison of their effectiveness in various nanophotonic applications. To this end, HPhPs in the lower MoO₃ reststrahlen band were found to have lifetimes up to about 9 ps (Figure 2f), which are about two orders of magnitude longer than SPP in Au at near-visible wavelengths [63, 64]. The lifetimes measured here, for HPhPs

propagating in MoO₃ on a gold-coated substrate, are longer than the lifetimes reported previously on SiO₂ surfaces (≈ 1.9 ps) [25]. This difference, in large part, is due to the long propagation lengths of the HPhPs (determined to be tip-launched) measured in these crystals.

Despite traveling within the volume of a host material, HPhPs are also sensitive to the surrounding media through their evanescently decaying external fields. These evanescent fields limit the range of HPhP interactions outside of the hyperbolic material, typically to a few tens of nm, similar to the decay range of SPPs [65, 66]. Consequently, variations in the local complex refractive index, such as near material discontinuities, can modify the dispersion, damping, and optical compression of HPhPs [67–71]. Measurements of a MoO₃ crystal deposited onto a linearly patterned SiO₂ substrate grating (alternating SiO₂ lines and 95-nm-deep trenches of nearly equal widths; see Figure 3c and Section 4 for details) enabled side-by-side examination of tip-launched HPhPs propagating in both substrate-supported and suspended regions, revealing clear differences (Figure 3b and d). In suspended regions, HPhP fringes extend farther from the crystal edges and have lower optical compressions than HPhPs propagating in regions of the MoO₃ crystal in direct contact with the SiO₂ substrate. Quantitative comparison of PTIR absorption profiles measured at 910 cm⁻¹, averaged along narrow bands centered within each region, reveals that HPhPs in suspended regions propagate with wavelengths $\approx 1.5\times$ longer than in regions in direct contact with the substrate (Figure 3f). Extension of this analysis to other excitation wavelengths yields the dispersion relations and propagation parameters characterizing HPhPs in each of these regions (Figure S4), including lifetimes of up to ≈ 12 ps in suspended regions of the MoO₃ crystal (Figure 3h). We hypothesize that the shortened lifetimes for HPhPs propagating in the supported regions (≈ 5 ps) are a result of dissipative interactions with the SiO₂ substrate, which is characterized by a broad and strong (i.e., large imaginary refractive index) phonon resonance near 1075 cm⁻¹. These interactions are not experienced as strongly within suspended MoO₃ regions. Unlike the sharp, step-like changes in the grating topography, the HPhP fringes in the PTIR absorption maps exhibit gradual transitions from a compact, high spatial frequency arrangements in the SiO₂-contacted regions of the flake, to more diffuse, low spatial frequency arrangements in suspended regions. The extent over which these transitions occur illustrates the lateral range of the gradually weakening influence of the supporting substrate on HPhPs propagation, which is proportional to the polaritonic wavelength. As expected, these transitions become sharper for HPhPs with higher optical

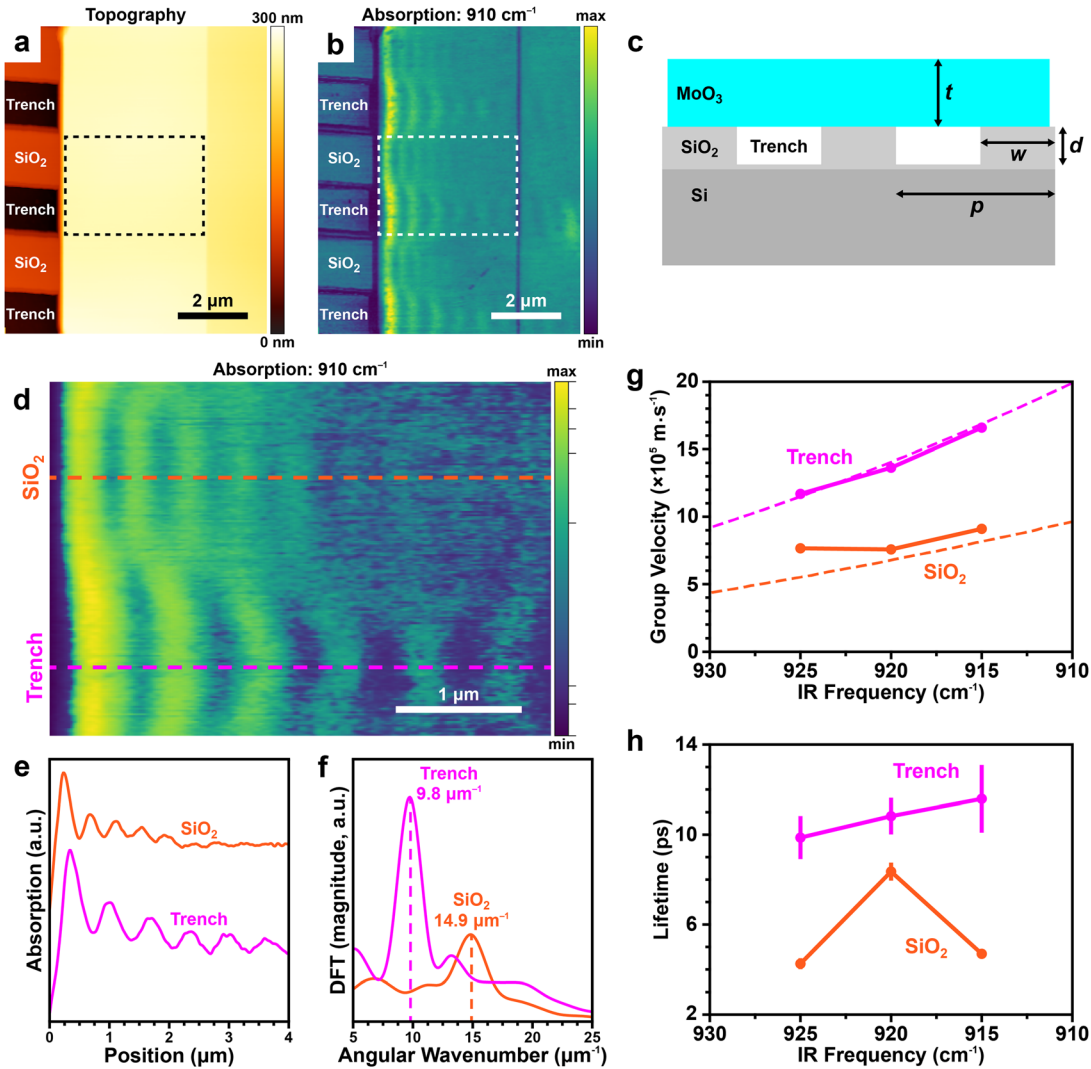


Figure 3: Topographically patterned substrates enable control over hyperbolic phonon polariton (HPhP) propagation.

(a) Topography, (b) photothermal induced resonance (PTIR) absorption map at 910 cm^{-1} , and (c) schematic of a MoO_3 flake (thickness $t \approx 185\text{ nm}$) deposited on one-dimensional SiO_2 grating lines (width $w \approx 1.4\text{ }\mu\text{m}$, pitch $p \approx 3\text{ }\mu\text{m}$) separated by trenches of depth $d \approx 95\text{ nm}$. (d) Magnified PTIR absorption map at 910 cm^{-1} of the region enclosed by the dashed rectangles in (a) and (b). (e) Averaged (165-nm-wide) absorption line profiles measured along the indicated paths in (d). (f) Magnitudes of the discrete Fourier transforms (DFTs) of the absorption profiles shown in (e); cubic spline interpolation plotted. Peaks in the respective DFT power spectra indicate that HPhPs propagate with higher optical compressions ($\approx 1.5\times$) in regions of the MoO_3 flake in direct contact with the SiO_2 substrate compared to suspended regions, above the trenches. (g) Group velocities and corresponding (h) HPhP lifetimes. Dashed lines in (g) represent the theoretical group velocity of first order, edge-launched HPhPs. Error bars in (g) and (h) represent uncertainties in the mean values, propagated from least-squares fit covariance matrices. Note that a non-linear color scale is used in (d) with bands of approximately equal changes in absorption intensity indicated with tick marks along the right side of the color bar.

compressions (i.e., shorter polariton wavelengths) [67]. These results demonstrate that substrate engineering is a viable strategy for controlling HPhP propagation with direct, localized effects on HPhP lifetimes and optical compressions, in agreement with previous studies [69, 70]. Since we detect no significant deformations of the MoO_3 crystal due to uneven surface contact or mechanical loading by the probe tip in the suspended regions, we

expect lattice strain to play a negligible role in the variations in HPhP propagation observed here.

The PTIR measurements presented here also reveal crystal defects and buried contaminants that are imperceptible to examinations of only the exposed sample topography or that would be difficult to detect with primarily surface-sensitive methods. Unlike s-SNOM, for which the sensitivity of the tip-scattered light decreases

rapidly as a function of the depth [33, 72], PTIR is capable of detecting subsurface features at depths up to a few μm , comparable with the IR light penetration depth [33, 34, 73]. Figure 4 shows PTIR absorption maps at 985 and 910 cm^{-1} of the same MoO₃ flake seen in Figure 3 (different location), revealing relatively strong absorption in regions localized over trenches in the substrate. Absorption spectra measured on these features exhibit a distinctive peak at $\approx 1264 \text{ cm}^{-1}$ that we attribute to the Si-CH₃ asymmetric deformation of polydimethylsiloxane (PDMS) residue [40]. Since no significant topographic features were observed on the exposed surface, we conclude that these features represent PDMS contaminants trapped primarily in the trenches beneath the crystal, derived from the polymer stamp used to prepare the sample (see Section 4). We observe HPhPs propagating in the MoO₃ crystal directly above the PDMS contaminants (Figure 4b). However, due to the PDMS background absorption, the effect of PDMS on HPhP propagation could not be quantified properly here. In addition to extrinsic contamination, seemingly intrinsic defects present in some MoO₃ crystals were also observed in PTIR absorption maps that do not correspond to obvious topographic features and with apparent negligible affect HPhP propagation (see Figure 1 and Supplementary materials Section S6.1).

3 Conclusions

In summary, PTIR absorption maps visualize HPhPs propagating in exfoliated $\alpha\text{-MoO}_3$ single crystals. By combining real-space PTIR images and Fourier analyses, we determined the polariton dispersion relations, propagation lengths, lifetimes, and group velocities in MoO₃ crystals. Long HPhP lifetimes, in excess of 10 ps, were measured for HPhPs propagating in MoO₃ with optical compressions $>30\times$. The effects of substrate morphology were tested by comparing HPhP propagation in regions of a MoO₃ flake, deposited on a grating substrate, that were either suspended or in direct contact with SiO₂. Polaritons in suspended regions of the flake were found to propagate farther, with longer lifetimes ($\approx 2\times$) and lower optical compressions ($\approx 1.5\times$), than those in regions in direct contact with the substrate. Additionally, by leveraging the ability of PTIR to sense subsurface features, we detected and identified the composition of contaminants (PDMS) beneath regions of a MoO₃ flake, which originated from the sample preparation procedure. We also observed that some intrinsic crystal defects in MoO₃ had negligible impacts on HPhP propagation. This work demonstrates the versatility of PTIR for nanophotonic measurements of HPhPs, which

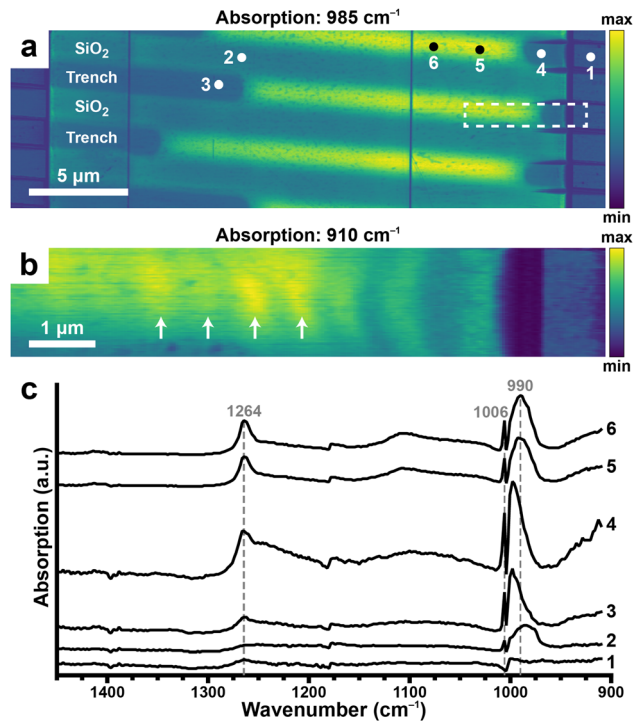


Figure 4: Photothermal induced resonance (PTIR) reveals trapped contaminants that can influence hyperbolic phonon polariton (HPhP) propagation and imaging. Absorption maps at (a) 985 cm^{-1} and at (b) 910 cm^{-1} , magnified region from (a), of the same MoO₃ crystal shown in Figure 3 (but at a different location), supported by a SiO₂/Si grating. Relatively strong, localized absorption features (absent in topography) reveal contaminants trapped beneath the MoO₃ flake. (c) Absorption spectra measured at locations one to six indicated in (a) identify the contaminants as polydimethylsiloxane (PDMS), derived from sample preparation. The contaminants underneath the MoO₃ flake affect the HPhP propagation and change the apparent spacing between successive fringes, indicated by arrows in (b), compared with those observed in uncontaminated regions (e.g., Figure 3b and d). Topography maps acquired simultaneously with (a) and (b) are available in the Supplementary material (Figure S6).

provides a useful complement to s-SNOM studies. Furthermore, leveraging substrate morphology and material composition, as demonstrated here, represents a viable technique that enhances the ability to engineer and to control HPhP propagation in other nanophotonic systems.

4 Methods

4.1 Synthesis of single-crystalline $\alpha\text{-MoO}_3$

Single-crystalline flakes of $\alpha\text{-MoO}_3$ were grown by the physical vapor transport method. At one end of an evacuated quartz ampoule, MoO₃ polycrystalline powder (99.9995%) was heated to a temperature of $\approx 830 \text{ }^\circ\text{C}$, which is slightly higher than its melting point ($\approx 795 \text{ }^\circ\text{C}$), for

2 h. Single-crystalline MoO₃ flakes formed at the cooler end of the ampoule, which was maintained at a temperature of ≈ 700 °C.

4.2 Exfoliation and deposition of MoO₃

Flakes of MoO₃ were exfoliated as single crystals directly onto uniform, gold-coated (≈ 100 nm) glass substrates by using standard techniques [74]. Alternatively, for surface morphology experiments, exfoliation of MoO₃ was carried out onto PDMS stamps, which were then used to transfer the crystals onto SiO₂/Si gratings. The gratings were characterized by 1D lines of SiO₂ (width ≈ 1.4 μm , pitch ≈ 3 μm) separated by trenches (depth ≈ 95 nm), on an n-doped (conductivity ≈ 4.5 Ω cm) Si substrate with native oxide (≈ 1 nm), as depicted schematically in Figure 3c. Stamps, carrying exfoliated MoO₃ flakes, were aligned and brought into contact with the grating surface and held while heated to temperatures of ≈ 40 °C. Slowly separating the stamp from the substrate resulted in the MoO₃ being transferred from the PDMS to grating surface. Due to the reduced contact area between a flake and the grating substrate, deposition from the stamp to the grating typically was more challenging than deposition onto a flat surface. Consequently, repeated iterations of the deposition procedure (contact, heating, removal) were sometimes needed before transferring the MoO₃ to the grating successfully. As a result, some portions of the grating were repeatedly contacted by the stamp and became contaminated. Such contaminated portions were later covered with the transferred flake.

4.3 Photothermal induced resonance measurements

4.3.1 Phonon polariton imaging and nanoscale point spectroscopy:

All PTIR measurements in this work were made by using a resonance enhanced excitation scheme [75] with a gold-coated Si probe (nominal spring constant 0.07–0.4 N/m and first resonance frequency in air of 13 kHz \pm 4 kHz) operated in contact mode. A quantum cascade laser (QCL) array with a tunable pulse repetition rate (1–2000 kHz) and wavelength (910–1905 cm⁻¹) was used to illuminate a region of the sample (diameter ≈ 50 μm) around the probe tip. Laser light (p-polarized) was obliquely incident upon flakes of MoO₃ such that multiple edges were illuminated at once. A phase-locked loop with 50–100 kHz bandwidth was used to maintain the resonant excitation condition by adjusting the laser pulse repetition rate to match one of the contact-resonance modes of the cantilever (≈ 400 kHz), leading to a $Q/2\pi$ amplification of the PTIR signal, where Q is the quality factor of the cantilever mode [75]. Absorption maps were measured by scanning the probe while illuminating the sample at a constant wavelength. Alternatively, by maintaining the probe at a fixed location and varying the wavelength of the incident IR light, point spectra were obtained by computing the ratios of the measured PTIR response to the laser output intensity at each wavelength (background spectrum). Since the QCL array consists of four chips, spectral artifacts can be introduced at the transitions between these chips (1179, 1473, and 1689 cm⁻¹) where the laser output intensity is relatively low. To enable easier side-by-side comparison, spectra were normalized to have a common intensity at one of these artifacts (1179 cm⁻¹), plotted with a common scale, and vertically offset for clarity.

4.3.2 Image processing and analysis: Simultaneously acquired topography and PTIR absorption map pairs were analyzed with

customized processing routines to obtain estimates of HPhP propagation characteristics. The positions of MoO₃ crystal edges were determined by applying a Canny edge detection algorithm to flattened (plane-subtracted) topographs, enabling image segmentation into regions inside and outside of the analyzed flakes. One-dimensional absorption profiles were obtained from the 2D maps by column-wise (i.e., along the direction of the crystal edges) averaging, with only those portions inside the flake boundaries considered in the subsequent processing steps. To reduce the influence of low spatial frequency variations (e.g., ‘pink noise’) on HPhP analysis, exponentially decaying lines of best fit and arithmetic means were subtracted from the averaged absorption profiles. Excited HPhP modes within MoO₃ crystals were identified by peaks in the discrete Fourier transforms of these corrected absorption profiles. The wavenumbers were estimated from cubic spline interpolations of the resulting power spectra. These wavenumbers, as well as other characteristics of the detected HPhP modes, were refined by fitting the model expressed by Equation (1) to filtered absorption profiles; see Supplementary material S7. Filter functions exponentially damped absorption signals with spatial frequencies below about 65 % of the first detected peak position and above angular wavenumbers of about 100 μm^{-1} , while uniformly passing signals between these bounds. Group velocities were estimated by computing the numerical derivative of the HPhP dispersion relationship (e.g., Figure 2d) by using the symmetric finite difference method. Reported uncertainties for all quantities represent one standard deviation in the mean value. In the cases of quantities derived from least-squares fits, these values are from the propagated uncertainties obtained from the covariance matrices. The optimized fitting parameters were determined independently for each PTIR image. Therefore, the reported error bars only estimate fitting uncertainties of a single image (single IR wavelength) and do not account for image-to-image variability.

Acknowledgments: J.J.S. acknowledges support under the Corporative Research Agreement Award 70NANB14H209, through the University of Maryland. S.T.L. acknowledges support from the National Institute of Standards and Technology grant 70NANB16H170.

Author contributions: All the authors have accepted responsibility for the entire content of this submitted manuscript and approved submission.

Research funding: J.J.S. received financial support from the Corporative Research Agreement Award under the grant 70NANB14H209, through the University of Maryland and S.T.L. received financial support from the National Institute of Standards and Technology under the grant 70NANB16H170.

Conflict of interest statement: The authors declare no conflicts of interest regarding this article.

References

- [1] S. Lal, S. Link, and N. J. Halas, “Nano-optics from sensing to waveguiding,” *Nat. Photonics*, vol. 1, no. 11, pp. 641–648, 2007.

- [2] N. J. Halas, S. Lal, W.-S. Chang, S. Link, and P. Nordlander, "Plasmons in strongly coupled metallic nanostructures," *Chem. Rev.*, vol. 111, no. 6, pp. 3913–3961, 2011.
- [3] T. G. Mayerhöfer and J. Popp, "Periodic array-based substrates for surface-enhanced infrared spectroscopy," *Nanophotonics*, vol. 7, no. 1, pp. 39–79, 2018.
- [4] F. Neubrech, C. Huck, K. Weber, A. Pucci, and H. Giessen, "Surface-enhanced infrared spectroscopy using resonant nanoantennas," *Chem. Rev.*, vol. 117, no. 7, pp. 5110–5145, 2017.
- [5] J. Lee, K. T. Crampton, N. Tallarida, and V. A. Apkarian, "Visualizing vibrational normal modes of a single molecule with atomically confined light," *Nature*, vol. 568, no. 7750, p. 78, 2019.
- [6] W. Bogaerts, R. Baets, P. Dumon, et al., "Nanophotonic waveguides in silicon-on-insulator fabricated with CMOS technology," *J. Lightwave Technol.*, vol. 23, no. 1, p. 401, 2005.
- [7] D. K. Gramotnev and S. I. Bozhevolnyi, "Plasmonics beyond the diffraction limit," *Nat. Photonics*, vol. 4, no. 2, pp. 83–91, 2010.
- [8] Z. Han and S. I. Bozhevolnyi, "Radiation guiding with surface plasmon polaritons," *Rep. Prog. Phys.*, vol. 76, no. 1, p. 016402, 2012.
- [9] A. Lesuffleur, L. K. S. Kumar, and R. Gordon, "Enhanced second harmonic generation from nanoscale double-hole arrays in a gold film," *Appl. Phys. Lett.*, vol. 88, no. 26, p. 261104, 2006.
- [10] M. A. Foster, A. C. Turner, M. Lipson, and A. L. Gaeta, "Nonlinear optics in photonic nanowires," *Opt. Express*, vol. 16, no. 2, pp. 1300–1320, 2008.
- [11] F. Le, D. W. Brandl, Y. A. Urzhumov, et al., "Metallic nanoparticle arrays: a common substrate for both surface-enhanced Raman scattering and surface-enhanced infrared absorption," *ACS Nano*, vol. 2, no. 4, pp. 707–718, 2008.
- [12] J. F. Li, Y. F. Huang, Y. Ding, et al., "Shell-isolated nanoparticle-enhanced Raman spectroscopy," *Nature*, vol. 464, no. 7287, pp. 392–395, 2010.
- [13] Y. Zhong, S. D. Malagari, T. Hamilton, and D. M. Wasserman, "Review of mid-infrared plasmonic materials," *J. Nanophotonics*, vol. 9, no. 1, p. 093791, 2015.
- [14] J. D. Caldwell, L. Lindsay, V. Giannini, et al., "Low-loss, infrared and terahertz nanophotonics using surface phonon polaritons," *Nanophotonics*, vol. 4, no. 1, pp. 44–68, 2015.
- [15] D. T. Ha, D. T. Thuy, V. T. Hoa, T. T. Van, and N. A. Viet, "On the theory of three types of polaritons (phonon, exciton and plasmon polaritons)," *J. Phys. Conf. Ser.*, vol. 865, p. 012007, 2017.
- [16] L. Ferrari, C. Wu, D. Lepage, X. Zhang, and Z. Liu, "Hyperbolic metamaterials and their applications," *Prog. Quant. Electron.*, vol. 40, pp. 1–40, 2015.
- [17] T. Low, A. Chaves, J. D. Caldwell, et al., "Polaritons in layered two-dimensional materials," *Nat. Mater.*, vol. 16, no. 2, pp. 182–194, 2017.
- [18] S. Dai, Z. Fei, Q. Ma, et al., "Tunable phonon polaritons in atomically thin van der Waals crystals of boron nitride," *Science*, vol. 343, no. 6175, pp. 1125–1129, 2014.
- [19] A. J. Giles, S. Dai, I. Vurgaftman, et al., "Ultralow-loss polaritons in isotopically pure boron nitride," *Nat. Mater.*, vol. 17, no. 2, pp. 134–139, 2018.
- [20] P. Li, M. Lewin, A. V. Kretinin, et al., "Hyperbolic phonon-polaritons in boron nitride for near-field optical imaging and focusing," *Nat. Commun.*, vol. 6, p. 7507, 2015.
- [21] S. Dai, Q. Ma, T. Andersen, et al., "Subdiffractional focusing and guiding of polaritonic rays in a natural hyperbolic material," *Nat. Commun.*, vol. 6, p. 6963, 2015.
- [22] J. D. Caldwell, A. V. Kretinin, Y. Chen, et al., "Sub-diffractional volume-confined polaritons in the natural hyperbolic material hexagonal boron nitride," *Nat. Commun.*, vol. 5, p. 5221, 2014.
- [23] Z. Shi, H. A. Bechtel, S. Berweger, et al., "Amplitude- and phase-resolved nanospectral imaging of phonon polaritons in hexagonal boron nitride," *ACS Photonics*, vol. 2, no. 7, pp. 790–796, 2015.
- [24] Z. Zheng, J. Chen, Y. Wang, et al., "Highly confined and tunable hyperbolic phonon polaritons in van der Waals semiconducting transition metal oxides," *Adv. Mater.*, vol. 30, no. 13, p. 1705318, 2018.
- [25] W. Ma, P. Alonso-González, S. Li, et al., "In-plane anisotropic and ultra-low-loss polaritons in a natural van der Waals crystal," *Nature*, vol. 562, no. 7728, pp. 557–562, 2018.
- [26] Z. Zheng, N. Xu, S. L. Oscurato, et al., "A mid-infrared biaxial hyperbolic van der Waals crystal," *Sci. Adv.*, vol. 5, no. 5, p. eaav8690, 2019.
- [27] G. Hu, J. Shen, C.-W. Qiu, A. Alù, and S. Dai, "Phonon polaritons and hyperbolic response in van der Waals materials," *Adv. Opt. Mater.*, vol. 8, no. 5, p. 1901393, 2020.
- [28] C. Luo, X. Guo, H. Hu, et al., "Probing polaritons in 2D materials," *Adv. Opt. Mater.*, vol. 8, no. 5, p. 1901416, 2020.
- [29] X. G. Xu, B. G. Ghamsari, J.-H. Jiang, et al., "One-dimensional surface phonon polaritons in boron nitride nanotubes," *Nat. Commun.*, vol. 5, no. 1, pp. 1–6, 2014.
- [30] S. Dai, Q. Ma, Y. Yang, et al., "Efficiency of launching highly confined polaritons by infrared light incident on a hyperbolic material," *Nano Lett.*, vol. 17, no. 9, pp. 5285–5290, 2017.
- [31] D. Nowak, W. Morrison, H. K. Wickramasinghe, et al., "Nanoscale chemical imaging by photoinduced force microscopy," *Sci. Adv.*, vol. 2, no. 3, p. e1501571, 2016.
- [32] A. Ambrosio, L. A. Jauregui, S. Dai, et al., "Mechanical detection and imaging of hyperbolic phonon polaritons in hexagonal boron nitride," *ACS Nano*, vol. 11, no. 9, pp. 8741–8746, 2017.
- [33] A. Centrone, "Infrared imaging and spectroscopy beyond the diffraction limit," *Annu. Rev. Anal. Chem.*, vol. 8, no. 1, pp. 101–126, 2015.
- [34] D. Korouski, A. Dazzi, R. Zenobi, and A. Centrone, "Infrared and Raman chemical imaging and spectroscopy at the nanoscale," *Chem. Soc. Rev.*, vol. 49, no. 11, pp. 3315–3347, 2020.
- [35] L. V. Brown, M. Davanco, Z. Sun, et al., "Nanoscale mapping and spectroscopy of nonradiative hyperbolic modes in hexagonal boron nitride nanostructures," *Nano Lett.*, vol. 18, no. 3, pp. 1628–1636, 2018.
- [36] G. Ramer, M. Tuteja, J. R. Matson, et al., "High-Q dark hyperbolic phonon-polaritons in hexagonal boron nitride nanostructures," *Nanophotonics*, vol. 9, no. 6, pp. 1457–1467, 2020.
- [37] J. Chae, S. An, G. Ramer, et al., "Nanophotonic atomic force microscope transducers enable chemical composition and thermal conductivity measurements at the nanoscale," *Nano Lett.*, vol. 17, no. 9, pp. 5587–5594, 2017.
- [38] A. Deniset-Besseau, C. B. Prater, M.-J. Virolle, and A. Dazzi, "Monitoring TriAcylGlycerols accumulation by atomic force microscopy based infrared spectroscopy in *streptomyces* species for biodiesel applications," *J. Phys. Chem. Lett.*, vol. 5, no. 4, pp. 654–658, 2014.
- [39] K. Wieland, G. Ramer, V. U. Weiss, G. Allmaier, B. Lendl, and A. Centrone, "Nanoscale chemical imaging of individual chemotherapeutic cytarabine-loaded liposomal nanocarriers," *Nano Res.*, vol. 12, no. 1, pp. 197–203, 2019.

- [40] J. J. Schwartz, H.-J. Chuang, M. R. Rosenberger, et al., "Chemical identification of interlayer contaminants within van der Waals heterostructures," *ACS Appl. Mater. Interfaces*, vol. 11, no. 28, pp. 25578–25585, 2019.
- [41] G. Ramer, V. A. Aksyuk, and A. Centrone, "Quantitative chemical analysis at the nanoscale using the photothermal induced resonance technique," *Anal. Chem.*, vol. 89, no. 24, pp. 13524–13531, 2017.
- [42] A. Dazzi, F. Glotin, and R. Carminati, "Theory of infrared nanospectroscopy by photothermal induced resonance," *J. Appl. Phys.*, vol. 107, no. 12, p. 124519, 2010.
- [43] X. Ma, V. Beltran, G. Ramer, et al., "Revealing the distribution of metal carboxylates in oil paint from the micro- to nanoscale," *Angew. Chem. Int. Ed.*, vol. 58, no. 34, pp. 11652–11656, 2019.
- [44] J. Chae, Q. Dong, J. Huang, and A. Centrone, "Chloride incorporation process in CH₃NH₃PbI_{3-x}Cl_x perovskites via nanoscale bandgap maps," *Nano Lett.*, vol. 15, no. 12, pp. 8114–8121, 2015.
- [45] S. Morsch, Y. Liu, S. B. Lyon, and S. R. Gibbon, "Insights into epoxy network nanostructural heterogeneity using AFM-IR," *ACS Appl. Mater. Interfaces*, vol. 8, no. 1, pp. 959–966, 2016.
- [46] S. Kenkel, S. Mittal, and R. Bhargava, "Closed-loop atomic force microscopy-infrared spectroscopic imaging for nanoscale molecular characterization," *Nat. Commun.*, vol. 11, no. 1, p. 3225, 2020.
- [47] K. Kochan, D. Perez-Guaita, J. Pissang, et al., "In vivo atomic force microscopy-infrared spectroscopy of bacteria," *J. R. Soc. Interface*, vol. 15, no. 140, p. 20180115, 2018.
- [48] G. Ramer, F. S. Ruggeri, A. Levin, T. P. J. Knowles, and A. Centrone, "Determination of polypeptide conformation with nanoscale resolution in water," *ACS Nano*, vol. 12, no. 7, pp. 6612–6619, 2018.
- [49] V. Giliberti, R. Polito, E. Ritter, et al., "Tip-enhanced infrared difference-nanospectroscopy of the proton pump activity of bacteriorhodopsin in single purple membrane patches," *Nano Lett.*, vol. 19, no. 5, pp. 3104–3114, 2019.
- [50] L. Zhou and D. Kourouski, "Structural characterization of individual α -synuclein oligomers formed at different stages of protein aggregation by atomic force microscopy-infrared spectroscopy," *Anal. Chem.*, vol. 92, no. 10, pp. 6806–6810, 2020.
- [51] F. S. Ruggeri, B. Mannini, R. Schmid, M. Vendruscolo, and T. P. J. Knowles, "Single molecule secondary structure determination of proteins through infrared absorption nanospectroscopy," *Nat. Commun.*, vol. 11, no. 1, p. 2945, 2020.
- [52] K. Gallacher, R. W. Millar, D. J. Paul, et al., "Characterization of integrated waveguides by atomic-force-microscopy-assisted mid-infrared imaging and spectroscopy," *Opt. Express*, vol. 28, no. 15, pp. 22186–22199, 2020.
- [53] A. M. Katzenmeyer, J. Chae, R. Kasica, G. Holland, B. Lahiri, and A. Centrone, "Nanoscale imaging and spectroscopy of plasmonic modes with the PTIR technique," *Adv. Opt. Mater.*, vol. 2, no. 8, pp. 718–722, 2014.
- [54] A. B. Khanikaev, N. Arju, Z. Fan, et al., "Experimental demonstration of the microscopic origin of circular dichroism in two-dimensional metamaterials," *Nat. Commun.*, vol. 7, no. 1, pp. 1–8, 2016.
- [55] J. Chae, B. Lahiri, and A. Centrone, "Engineering near-field SEIRA enhancements in plasmonic resonators," *ACS Photonics*, vol. 3, no. 1, pp. 87–95, 2016.
- [56] B. Lahiri, G. Holland, V. Aksyuk, and A. Centrone, "Nanoscale imaging of plasmonic hot spots and dark modes with the photothermal-induced resonance technique," *Nano Lett.*, vol. 13, no. 7, pp. 3218–3224, 2013.
- [57] V. Aksyuk, B. Lahiri, G. Holland, and A. Centrone, "Near-field asymmetries in plasmonic resonators," *Nanoscale*, vol. 7, no. 8, pp. 3634–3644, 2015.
- [58] M. C. Rao, K. Ravindranadh, A. Kasturi, and M. S. Shekhawat, "Structural stoichiometry and phase transitions of MoO₃ thin films for solid state microbatteries," *Res. J. Recent Sci.*, vol. 2, no. 4, pp. 67–73, 2013.
- [59] M. A. Py, Ph. E. Schmid, and J. T. Vallin, "Raman scattering and structural properties of MoO₃," *Nuov. Cim. B*, vol. 38, no. 2, pp. 271–279, 1977.
- [60] Z. Sun, Á. Gutiérrez-Rubio, D. N. Basov, and M. M. Fogler, "Hamiltonian optics of hyperbolic polaritons in nanogranules," *Nano Lett.*, vol. 15, no. 7, pp. 4455–4460, 2015.
- [61] A. Ambrosio, M. Tamagnone, K. Chaudhary, et al., "Selective excitation and imaging of ultraslow phonon polaritons in thin hexagonal boron nitride crystals," *Light Sci. Appl.*, vol. 7, no. 1, pp. 1–9, 2018.
- [62] E. Yoxall, M. Schnell, A. Y. Nikitin, et al., "Direct observation of ultraslow hyperbolic polariton propagation with negative phase velocity," *Nat. Photonics*, vol. 9, no. 10, pp. 674–678, 2015.
- [63] C. Ropers, D. J. Park, G. Stibenz, et al., "Femtosecond light transmission and subradiant damping in plasmonic crystals," *Phys. Rev. Lett.*, vol. 94, no. 11, p. 113901, 2005.
- [64] J. Li, H. Lu, D. Y. Lei, et al., "Dependence of surface plasmon lifetimes on the hole size in two-dimensional metallic arrays," *Appl. Phys. Lett.*, vol. 94, no. 18, p. 183112, 2009.
- [65] M. Autore, P. Li, I. Dolado, et al., "Boron nitride nanoresonators for phonon-enhanced molecular vibrational spectroscopy at the strong coupling limit," *Light Sci. Appl.*, vol. 7, no. 4, p. 17172, 2018.
- [66] A. V. Zayats, I. I. Smolyaninov, and A. A. Maradudin, "Nano-optics of surface plasmon polaritons," *Phys. Rep.*, vol. 408, no. 3, pp. 131–314, 2005.
- [67] K. Chaudhary, M. Tamagnone, M. Rezaee, et al., "Engineering phonon polaritons in van der Waals heterostructures to enhance in-plane optical anisotropy," *Sci. Adv.*, vol. 5, no. 4, p. eaau7171, 2019.
- [68] K. S. Kim, D. Trajanoski, K. Ho, et al., "The effect of adjacent materials on the propagation of phonon polaritons in hexagonal boron nitride," *J. Phys. Chem. Lett.*, vol. 8, no. 13, pp. 2902–2908, 2017.
- [69] S. Dai, J. Quan, G. Hu, et al., "Hyperbolic phonon polaritons in suspended hexagonal boron nitride," *Nano Lett.*, vol. 19, no. 2, pp. 1009–1014, 2019.
- [70] A. Fali, S. T. White, T. G. Folland, et al., "Refractive index-based control of hyperbolic phonon-polariton propagation," *Nano Lett.*, vol. 19, no. 11, pp. 7725–7734, 2019.
- [71] T. G. Folland, A. Fali, S. T. White, et al., "Reconfigurable infrared hyperbolic metasurfaces using phase change materials," *Nat. Commun.*, vol. 9, no. 1, pp. 1–7, 2018.
- [72] T. Taubner, F. Keilmann, and R. Hillenbrand, "Nanoscale-resolved subsurface imaging by scattering-type near-field optical microscopy," *Opt. Express*, vol. 13, no. 22, pp. 8893–8899, 2005.

- [73] B. Lahiri, G. Holland, and A. Centrone, “Chemical imaging beyond the diffraction limit: experimental validation of the PTIR technique,” *Small*, vol. 9, no. 3, pp. 439–445, 2013.
- [74] J. A. Hagmann, S. T. Le, C. A. Richter, and D. G. Seiler, “Advanced experimental methods for low-temperature magnetotransport measurement of novel materials,” *J. Vis. Exp.*, vol. 107, p. e53506, 2016.
- [75] F. Lu, M. Jin, and M. A. Belkin, “Tip-enhanced infrared nanospectroscopy via molecular expansion force detection,” *Nat. Photonics*, vol. 8, no. 4, pp. 307–312, 2014.

Supplementary Material: The online version of this article offers supplementary material (<https://doi.org/10.1515/nanoph-2020-0640>).